

Supplementary Materials for

Imaging quantum spin Hall edges in monolayer WTe₂

Yanmeng Shi, Joshua Kahn, Ben Niu, Zaiyao Fei, Bosong Sun, Xinghan Cai, Brian A. Francisco, Di Wu, Zhi-Xun Shen, Xiaodong Xu, David H. Cobden, Yong-Tao Cui

*Corresponding author. Email: xuxd@uw.edu (X.X.); cobden@uw.edu (D.H.C.); yongtao.cui@ucr.edu (Y.-T.C.)

Published 8 February 2019, *Sci. Adv.* **5**, eaat8799 (2019)
DOI: 10.1126/sciadv.aat8799

This PDF file includes:

Section S1. Sample structures

Section S2. MIM images of monolayer WTe₂ flake

Section S3. Gate dependence of transport and MIM signals

Section S4. Simulation of the edge parameters

Section S5. The monolayer/bilayer WTe₂ flake in Fig. 3

Section S6. Gate dependence of internal cracks

Fig. S1. MIM-Im images taken for a large monolayer WTe₂ flake, overlaid on the optical image at $T = 8$ K and $B = 0$.

Fig. S2. Gate-dependent MIM images of the sample presented in Fig. 4C.

Fig. S3. Gate dependence of transport and MIM.

Fig. S4. Simulation of MIM near the edge.

Fig. S5. Conceptual model of the effects of disorder on the edge conduction in a magnetic field.

Fig. S6. AFM topography image of the monolayer WTe₂ flake presented in Fig. 3 (A to D).

Fig. S7. Gate dependence of internal cracks.

Table S1. Information of the monolayer WTe₂ samples presented in the main text.

Supplementary Materials

Section S1. Sample structures

Table S1. Information of the monolayer WTe₂ samples presented in the main text.

Figures where sample is presented	Upper hBN (nm)	Lower hBN (nm)	Contacts	Graphite gate
Fig. 1 B	~10	None	None	None
Fig. 2	~10	~8	Graphite, ~1-2 nm	None
Fig. 3 B	~10	None	None	None
Fig. 3 E , 3 F	~9	~15	Graphite, ~4 nm	None
Fig. 4 A , 4 B	~8	~60	Pt, ~8 nm	Yes
Fig. 4 C , 4 D	~20	~20	Pt, ~9 nm	Yes
Fig. 4 E , 4 F	~5	~29	Pt, ~8.5 nm	None

Section S2. MIM images of monolayer WTe₂ flake

Sample in Fig. 1 of the main text

The size of the monolayer WTe₂ flake presented in Fig. 1 of the main text is much larger than the scan size of our microscope. We imaged the majority of the flake through multiple scans. The MIM-Im images of these scans are overlaid on the optical image of the flake, plotted in fig. S1. The conducting edge state follows the entire edge of the flake.



Fig. S1. MIM-Im images taken for a large monolayer WTe₂ flake, overlaid on the optical image at $T = 8$ K and $B = 0$.

Sample in Fig. 4C of the main text

Figure S2 plots MIM images of the sample in Fig. 4C at different gate voltages. This sample has a nominal doping of 1.3% of Re, though measurements did not suggest the doping was effective. It has many internal lines of complex patterns that divide the monolayer flake into multiple domains. Narrow regions around many contacts show a fully insulating behavior. As discussed in the main text, these regions are probably oxidized and thus have become a trivial insulator. Through the gate voltage dependence, it can be seen that some domains are electrically isolated from others (for example, the narrow domain in between the two contacts near the upper left

corner) and cannot be gated. The images in Fig. 4C of the main text correspond to the region around the two upper left contacts.

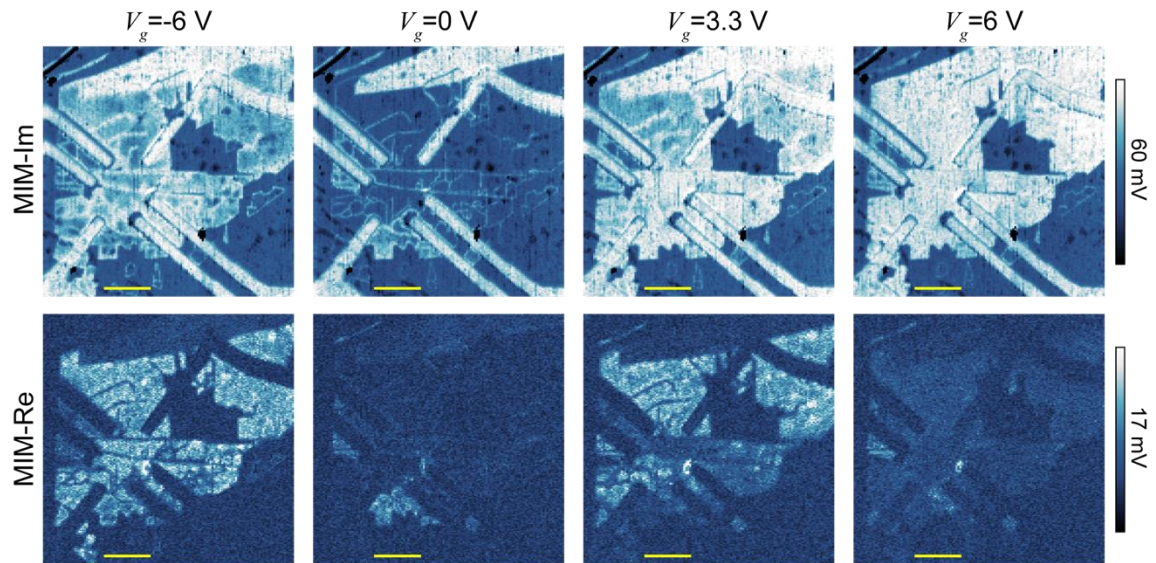


Fig. S2. Gate-dependent MIM images of the sample presented in Fig. 4C. MIM-Im (top row) and MIM-Re (bottom row). Scale bars are 3 μm .

Section S3. Gate dependence of transport and MIM signals

For the device presented in Fig. 2 of the main text, two-terminal transport and MIM measurements were performed simultaneously. In fig. S3, we plot the gate dependence of the two-terminal conductance, MIM-Im, and MIM-Re for both 0 T and 9 T, against the same gate voltage axis. The two-terminal conductance is strongly suppressed at 9 T, consistent with previous transport results (16, 19). The onset of higher conductance correlates well with the behavior of the MIM signals on both the p- and n-doped sides.

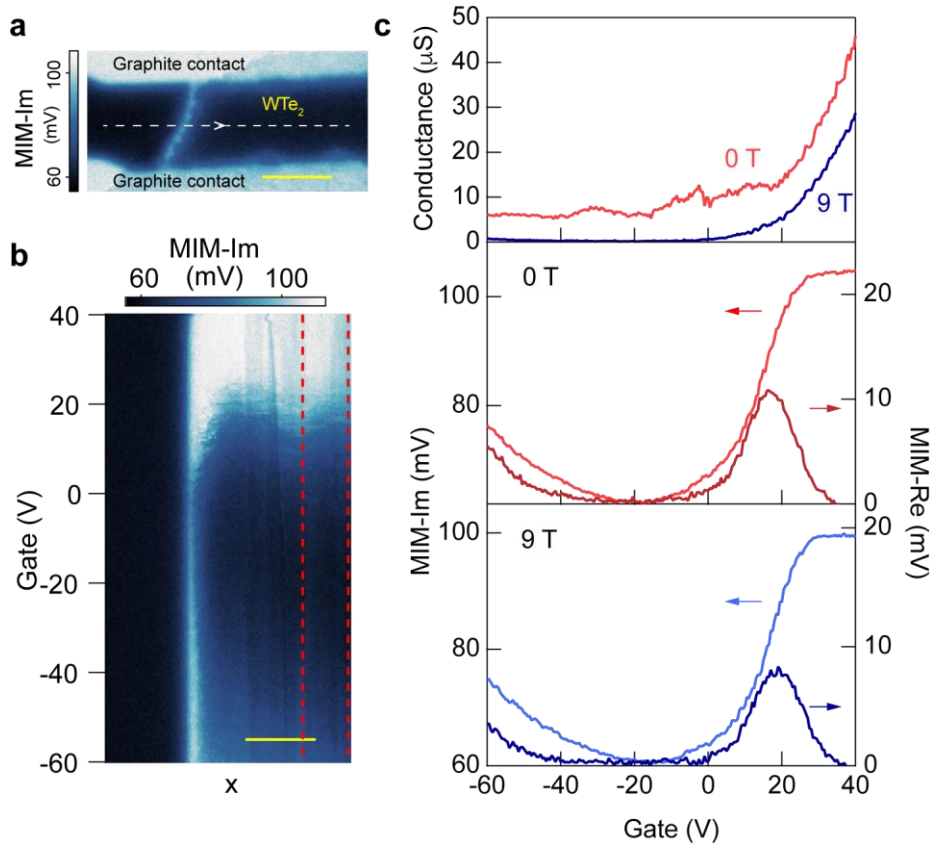


Fig. S3. Gate dependence of transport and MIM. (a) The MIM-Im image of the device at $B=0$. (b) The MIM-Im signal as a function of gate between -60 V and 40 V, taken along the dashed line marked in (a). (a) and (b) are the same data as presented in Fig. 2A and 2B. (c) Simultaneously measured two-terminal conductance (top), MIM-Im (the left axes of the middle and bottom panels) and MIM-Re (the right axes of the middle and bottom panels) signals as a function of gate voltage, at $B=0$ (middle) and 9 T (bottom). The MIM curves are averaged vertical linecuts from the gate dependence of the MIM-Im over the range marked by the red dashed line in (b). Measurement temperature is $T=5$ K. Scale bars are 1 μm .

Section S4. Simulation of the edge parameters

We simulate the MIM signals across the edge region and extract parameters of edge conduction based on a simplified model for the electromagnetic response of the edge mode. The finite element simulation is performed by commercial software COMSOL using its AC/DC module. As described in the Methods section of the main text, the MIM signals measured in the experiment correspond to $d(\text{MIM})/dz$, which removes an unknown background. In the simulation, $d(\text{MIM})/dz$ is calculated from the simulated tip-sample admittance as a function of tip-sample distance. There is then only one amplitude-scaling parameter involved in fitting the experimental data to the simulated results.

For the sample presented in Fig. 2 of the main text, most of the relevant geometrical parameters can be determined via atomic force microscopy and optical microscopy. The only unknown, yet critical, parameter is the size of the tip apex. This can be estimated through simulating the MIM signals across a well-defined reference edge in the sample structure, which in this case is the boundary between the graphite contact and the substrate, as illustrated in the fig. S4b. Figure S4c plots the simulated and measured MIM signals across this edge. A tip radius of 60 nm results in a good match of the simulated MIM-Im curve with the experimental data, both for the signal levels and for the profile of the transition. (Note that only one amplitude-scaling parameter is needed.)

Next, we model the edge state by a strip of uniform width w and uniform 2D conductivity σ_{2D} (fig. S4d). Using the same values of the tip radius and the amplitude-scaling parameter as determined previously, we find that the set of parameters that best fit both the 0 T and 9 T data are $w = 100$ nm, $\rho_{2D, 0T} = 200$ k Ω /sq and $\rho_{2D, 9T} = 540$ k Ω /sq (fig. S4e). The simulated parameters have a couple of discrepancies with our expectations. 1) The simulated edge width of 100 nm is larger than the expected width of ~ 10 nm for a QSH edge (6). The simulated MIM-Im curve for a 10 nm edge, with a resistivity value small enough to saturate the MIM-Im signal, does not match the measured peak height, as shown in the fig. S4e upper left panel. 2) The increase in the simulated edge resistivity under magnetic field is much smaller than the observation in the simultaneously taken transport shown in fig. S3.

Interpreting the simulated parameters of the edge conduction involves a number of challenges. To model the QSH edge correctly one needs to understand the response of the combination of nearly ballistic, one-dimensional edge conduction, which is intrinsically nonlocal, and any local conductivity contributions (e.g. from the bulk), to the oscillating voltage on the tip. The electric

fields may also be large enough to create nonlinear effects locally. The model used in the simulation is purely classical, accounting for only a local Ohmic conductivity. A better model of the edge response to the oscillating voltage on the tip is thus needed to take into account all the effects mentioned above; to the best of our knowledge, this situation has not been treated in the literature. In addition, the uniform edge profile could be oversimplified: there could be a non-uniform conductivity distribution near the edge due to disorder, seen as variations of peak strength and width in the MIM image in fig. S4b. In fact, such disorder can in part explain the second discrepancy mentioned above. A magnetic field opens an energy gap at the Dirac point of the edge state dispersion. When strong disorders are present, the edge will consist of alternating conducting and insulating segments, as illustrated in fig. S5a. Transport measures the effective series resistance along the edge which is dominated by the insulating segments (fig. S5b). A large increase in resistance (decrease in conductance) is thus expected. MIM, on the other hand, probes the edge conductivity from above the edge, and the edge contribution to the screening of tip electric field is equivalent to a parallel configuration of these segments, which is dominated by the nearest conducting portion (fig. S5c), hence the suppression is weaker. Further investigations are needed to address the important issues of the QSH edge width and the consequences of ballistic conduction and disorder.

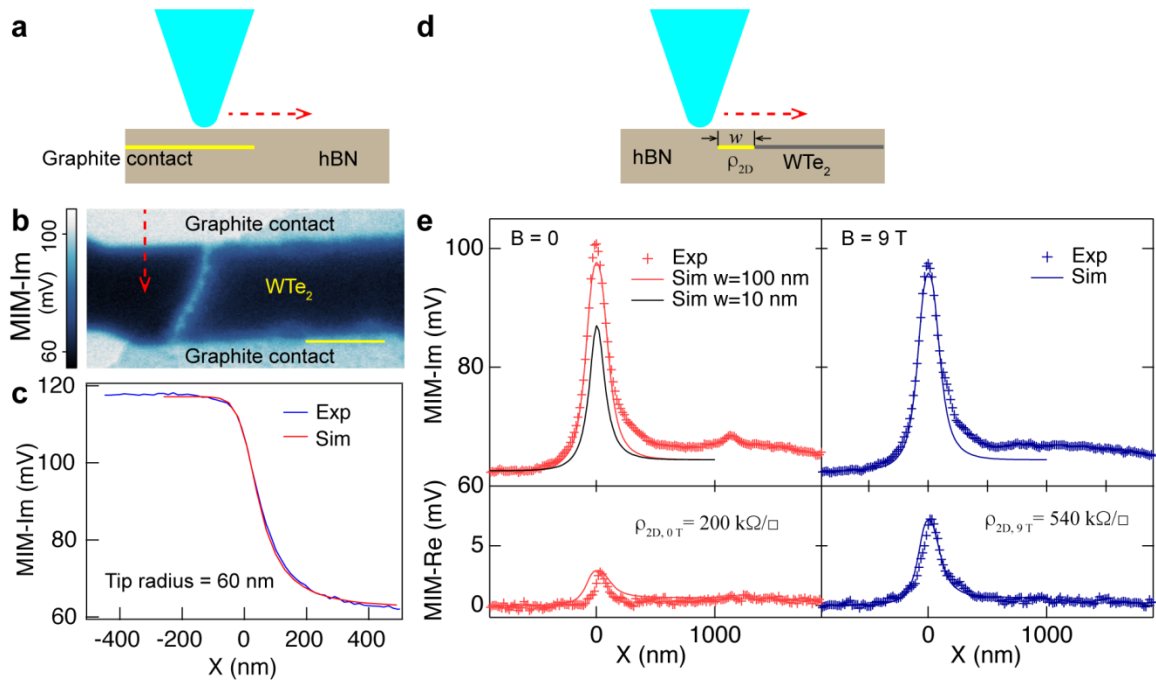


Fig. S4. Simulation of MIM near the edge. (a) Schematic of the structure near the boundary between graphite contact and the hBN. (b) MIM-Im image of the device, same as Fig. 2A in the main text. (c) Comparison of simulated and measured MIM-Im response across the graphite/hBN

boundary, as indicated by the red dashed line in (b). The scale bar is 1 μm . (d) Schematic of the model used to simulate the edge conduction. (e) Simulated MIM signals plotted together with the experimental data for $B=0$ (left) and $B=9$ T (right). The top row is the MIM-Im channel, and the bottom row is the MIM-Re channel. In each panel, the marks correspond to the experimental data, and the solid line is the result of the simulation. In the upper left panel, a simulated curve for edge width of 10 nm (black) is plotted along with the experimental data and a simulated curve for edge width of 100 nm (red).

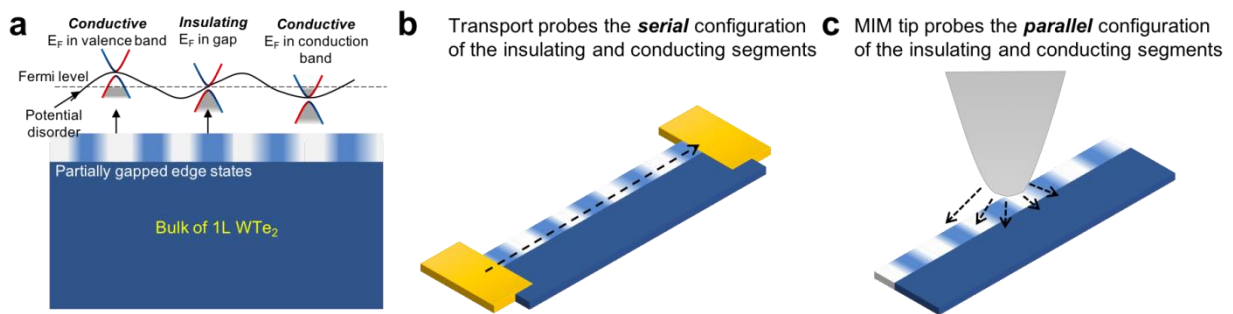


Fig. S5. Conceptual model of the effects of disorder on the edge conduction in a magnetic field. (a) Potential disorder causes variations of the conductivity along the edge, with resistive spots when the chemical potential is in the field-induced gap. (b & c) The probe geometries in transport and MIM measurement.

Section S5. The monolayer/bilayer WTe₂ flake in Fig. 3

Figure S6 plots the atomic force microscopy (AFM) topography image of the monolayer WTe₂ flake presented in Fig. 3A-3D in the main text. No topography features can be identified for the internal lines observed in the MIM image, ruling out the possibility of those lines being local folds or ripples. It also indicates that the gaps at these internal cracks are small compared to the typical AFM resolution (~ 10 nm). Therefore, the QSH edge modes on each side of the crack are spatially too close to be distinguished in the MIM image, so they appear as a single conducting line.

In addition, the folded bilayer has a bump near its boundary with the monolayer, which shows high conductivity in the MIM image (Fig. 3B in the main text). Based on our experience of many WTe₂ samples studied by MIM, we think this is a mildly degraded region which has a higher conductivity than the pristine bulk of monolayer and bilayer and tends to appear as a bump in topography. As discussed in the main text, the folded bilayer is topologically trivial and so does not host any conducting edge states. Therefore, an edge state would be expected at the boundary of bilayer and monolayer. However, the interaction between the two layers could affect the conductivity of an adjacent topological edge state, inducing backscattering that makes it highly resistive and thus not visible in the MIM image.

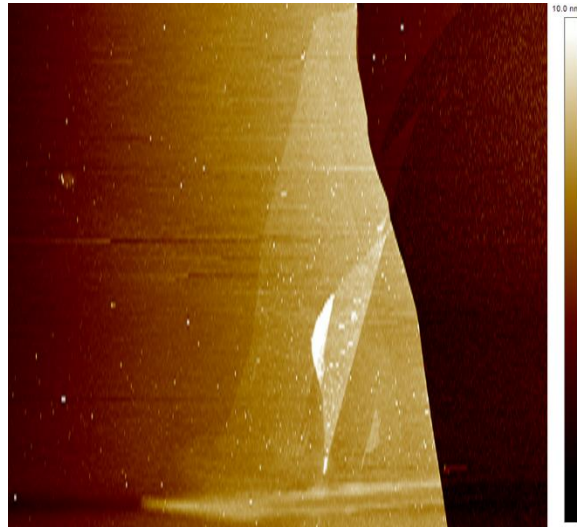


Fig. S6. AFM topography image of the monolayer WTe₂ flake presented in Fig. 3 (A to D). The scan size is 30 μm by 30 μm .

Section S6. Gate dependence of internal cracks

The gate dependence of the MIM signals across an internal crack and an exterior edge adjacent to each other are plotted in fig. S7. The behavior of the MIM signals at the internal crack is very similar to that of the exterior edge.

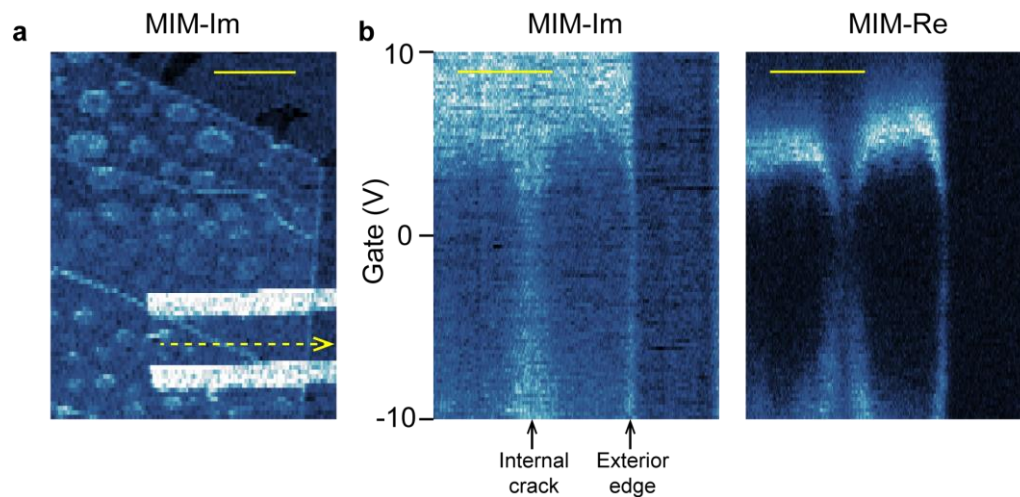


Fig. S7. Gate dependence of internal cracks. (a) MIM-Im image of a monolayer WTe₂ flake over a graphite gate. (b) MIM signal as a function of gate voltage between 10 V and -10 V, along a single line indicated by the yellow dashed line in (a) which crosses both an internal crack and the exterior edge. Scale bars are 2 μm .